Supporting Information: Electrochemical degradation of Pt_3Co nanoparticles investigated by off-lattice kinetic Monte Carlo simulations with machine-learned potentials

Jisu Jung,[†] Suyeon Ju,[†] Purun-hanul Kim,[†] Deokgi Hong,[†] Wonseok Jeong,[†,§] Jinhee Lee,[‡] Seungwu Han,[*,†,¶] and Sungwoo Kang[*,†,‖]

[†]*Department of Material Science and Engineering, Seoul National University, Seoul 08826, Korea*

[‡]*Fuel Cell Center, Hyundai Motor Company, Yongin 16891, Korea*

[¶]*Korea Institute for Advanced Study, Seoul 02455, Korea*

[§]*Present address: Lawrence Livermore National Laboratory, CA 94550, USA*

[‖]*Present address: Samsung Advanced Institute of Technology, Samsung Electronics, Suwon 16678, Korea*

E-mail: hansw@snu.ac.kr; kang1717@snu.ac.kr

The effect of solvation

Using the implicit solvation model,[S1,S2] we calculated the surface energy for Pt_3Co (100) surface (see TableS1). Due to the solvation effect, the surface energies are changed by 3–5 meV/Å^2, which are at most only 5.8% of surface energies. Additionally, we also checked the effect of solvation on vacancy formation energy for edge and vertex sites in a set of 10 distinct configurations, where most dissolution reactions could occur. For both Pt and Co atoms, the mean absolute errors in the vacancy formation energy due to solvation effects were 0.029 eV and 0.065 eV, respectively (see Figure S2). These values are an order of magnitude smaller than the vacancy formation energies themselves, confirming the negligible impact of solvation on our system.

Table S1: The surface energy of the Pt_3Co (100) slab system. N_X is the number of atoms X in the slab. Surface energies are written with a unit of meV/Å^2.

		N_{Pt}	N_{Co}	Without solvation effect	With solvation effect
Pt_3Co slab with Pt surface	Pristine	72	18	85	90
	With Pt vacancy	70	18	91	95
Pt_3Co slab with Pt:Co of 1:1 surface	Pristine	63	27	122	125
	With Pt vacancy	61	27	123	126
	With Co vacancy	63	25	122	125

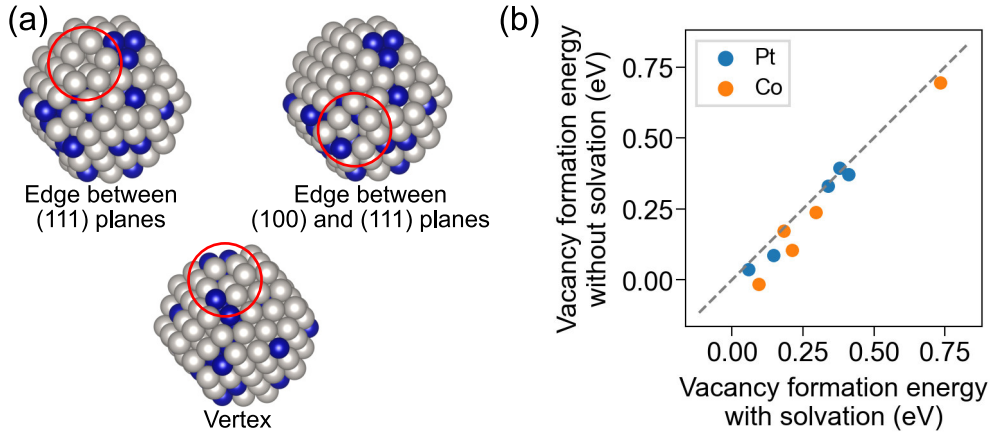

Figure S1: The effect of solvation on vacancy formation energy

Details of off-lattice kMC simulation

Dissolution

The dissolutions of atom X (X=Pt or Co) atoms from Pt–Co alloy nanoparticles are defined as follows:

$$\mathrm{Pt}_n\mathrm{Co}_m\mathrm{X} \rightarrow \mathrm{Pt}_n\mathrm{Co}_m + \mathrm{X}^{2+}\left(aq\right) + 2e^- \tag{1}$$

We obtain the activation barriers of dissolution reactions from the reaction energies using the Brønsted-Evans-Polanyi (BEP) relation which assumes that the change in the activation barrier is proportional to the reaction energy.[S3] Mathematically, it is defined by the following:

$$E_a = E_0 + \alpha\Delta E, \tag{2}$$

where E_a and ΔE are the activation barrier, and the energy difference, respectively, and E_0 and α are fitting parameters. ΔE can be calculated using the following equation:

$$\Delta E = E\left(\mathrm{Pt}_n\mathrm{Co}_m\right) + E\left(\mathrm{Pt}_n\mathrm{Co}_m\mathrm{X}\right) - 2eU_{\mathrm{app.}} + \mu\left(\mathrm{X}^{2+}\left(aq\right)\right) + 2\mu_{\mathrm{SHE}}\left(e^-\right) + T\Delta S_{\mathrm{diss.}}, \tag{3}$$

where $E\left(\mathrm{Pt}_n\mathrm{Co}_m\right)$ and $E\left(\mathrm{Pt}_n\mathrm{Co}_m\mathrm{X}\right)$ are the energies of $\mathrm{Pt}_n\mathrm{Co}_m$ and $\mathrm{Pt}_n\mathrm{Co}_m\mathrm{X}$ nanoparticles, respectively, and $eU_{\mathrm{app.}}$ is the energy of unit of electron charge, e, at applied voltage, $U_{\mathrm{app.}}$. $\mu\left(\mathrm{X}^{2+}\left(aq\right)\right)$ and $\mu_{\mathrm{SHE}}\left(e^-\right)$ are the chemical potentials of $\mathrm{X}^{2+}\left(aq\right)$ and electrons, respectively. T is the temperature, and $S_{\mathrm{diss.}}$ is the entropy of dissolution. $\mu\left(\mathrm{X}^{2+}\left(aq\right)\right) + 2\mu_{\mathrm{SHE}}\left(e^-\right)$ can be calculated using the standard electrode potential of bulk X atoms $E^0\left(\mathrm{X}\right)$:[S4]

$$\mu\left(\mathrm{X}^{2+}\left(aq\right)\right) + 2\mu_{\mathrm{SHE}}\left(e^-\right) = E\left(\mathrm{X}_{\mathrm{bulk}}\right) + 2eE^0\left(\mathrm{X}\right) \tag{4}$$

The parameters of the BEP relation are determined as follows. We assume that the reaction energy ΔE is affected by only the applied electrode potential, then α can be interpreted as the charge transfer coefficient in the Butler-Volmer equation. We adopt α as 0.3 from the

experiment which evaluated α from fitting to the potential dependence of dissolution rate of Pt_3Co nanoparticles.[S5] For a more accurate model, the parameter for the effect of the initial configuration and the parameter for the effect of the applied electrode potential on the activation energy should be dealt with separately.[S6] However, we assume that two different sources affect the activation energy to the same extent for simplicity. The remaining fitting parameters E_0 of each element are set to 0.5 eV for Pt and 1.0 eV for Co. An attempt frequency including the entropic term is set to 10^4 s^{-1}, which is typically used for dissolution reaction in other kMC simulations.[S7] We have conducted multiple kMC simulations to investigate the sensitivity of our results to the chosen parameters. Figures S2a and S2b illustrate the outcomes of sensitivity tests for the parameters α and E_0, respectively, pertaining to eq. S2. Notably, an increase in α to 0.4 barely influences the results, but a reduction to 0.2 demonstrates a noticeable shift. Regarding E_0, altering the value for Co has a minimal impact on the simulation, which can be attributed to the rapid removal of surface Co atoms at the start of the simulation. In contrast, altering E_0 of Pt produces considerable variations in the results. To determine if shifts of these parameters challenge the qualitative conclusions of our study, we charted the dissolution ratio evolution for nanoparticles of different shapes with the adjusted parameters in Figure S2c. As can be seen, the trend mirrors what we have presented in Figure 4c of the manuscript. We neglect the redeposition of dissolved atoms due to its lower frequency compared to the former two reactions that dominate the evolution of nanoparticles.[S8]

Diffusion

We constructed the spherical grid utilizing a Fibonacci lattice, which offers a nearly uniform distribution of grid points over the sphere, compared to the latitude–longitude lattice (see Figure S3).[S9]

For a predefined number of total points, N_{total}, the coordinates (X_i, Y_i, Z_i) for the i^{th} grid point are calculated using a radius r, as defined as follows:

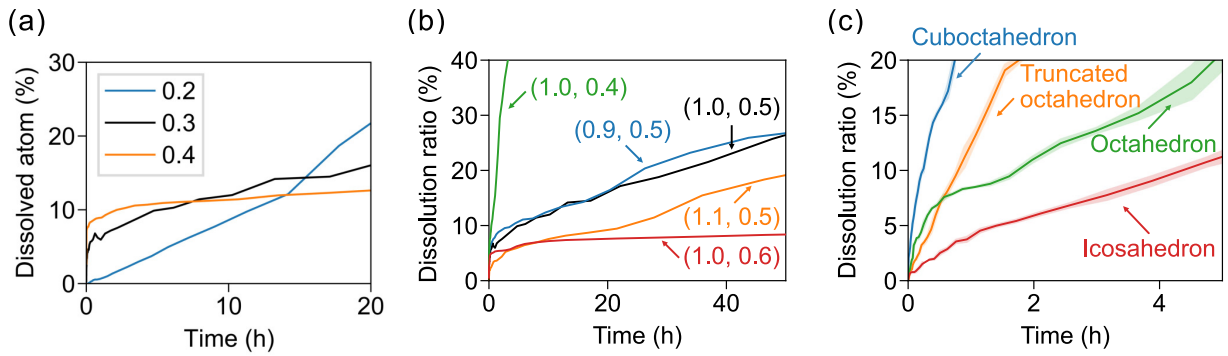

Figure S2: The effect of parameters for dissolution reaction. The dissolution ratios are shown for various (a) α and (b) E_0. E_0 for the Co and Pt atoms are written in parentheses as (E_0^{Co}, E_0^{Pt}) with an eV unit. (c) The effect of E_0 on durability on different shapes, where E_0 for the Co and Pt atoms are 1.1 and 0.4 eV, respectively.

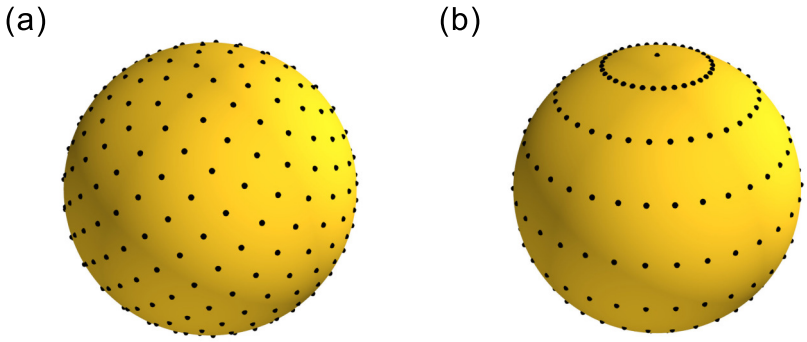

Figure S3: The identical number of grid points on the different lattices. (a) Fibonacci lattice. (b) latitude—longitude lattice.

$$X_i = r\sin(\theta_i)\cos(\varphi_i) \tag{5}$$

$$Y_i = r\sin(\theta_i)\sin(\varphi_i) \tag{6}$$

$$Z_i = r\cos(\theta_i), \tag{7}$$

where the θ_i and φ_i represent the azimuthal and zenith angles, respectively, and are given by:

$$\theta_i = \arccos\left(1 - \frac{2i+1}{N_{\mathrm{total}}}\right) \tag{8}$$

$$\varphi_i = \frac{1+\sqrt{5}}{2}\,(2i+1)\,\pi \tag{9}$$

Figure S3a shows the distribution of grid points for the Fibonacci lattices, each containing 360 points and a radius of 2.8 Å, which is the identical setting used in this study. This corresponds to a surface point density of 3.65 $Å^{-2}$. We did not allow finite thickness and only generated a grid on the surface of a sphere with a radius of 2.8 Å.

We establish a cutoff value for the minimum interatomic distances as 2.2 Å, based on the radial distribution function (RDF) derived from DFT MD simulations at 600 K for the disordered Pt–Co alloys (see Figure S4). The first peak in the RDF exhibits a shift with increasing Co concentration, indicative of a smaller atomic radius of Co relative to Pt. Despite this, strong repulsive interactions prevent any atoms from coming closer than 2.2 Å. Thus, we can assert with confidence that in our kMC simulations at 350 K, the interatomic distances will not fall below 2.2 Å.

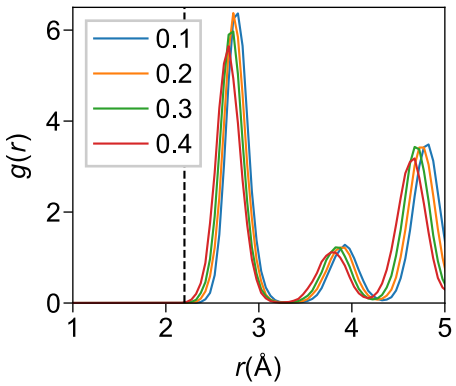

Figure S4: The radial distribution function of 600 K DFT MD trajectories of the disordered Pt–Co alloys at the Co compositions from 0.1 to 0.4. The dashed line represents the atomic distance at 2.2 Å.

Atoms with lower coordination numbers (CNs) frequently migrate to sites characterized by higher CNs. To validate this observation, we conducted targeted tests in which configurations with initial CNs of 3 or 4, originally omitted from our simulations, underwent geometry optimizations to evaluate if their CNs remained unchanged (see Figure S5). Remarkably, 78% of configurations that started with a CN of 3, and 62% that started with a CN of 4,

transitioned to higher-CN states upon relaxation. We further observe that these high-CN states are also accessible from our initial grid points characterized by high CNs. Therefore, the exclusion of low-coordinated sites does not compromise the ability of our method to model effective reactions while offering significant computational efficiency.

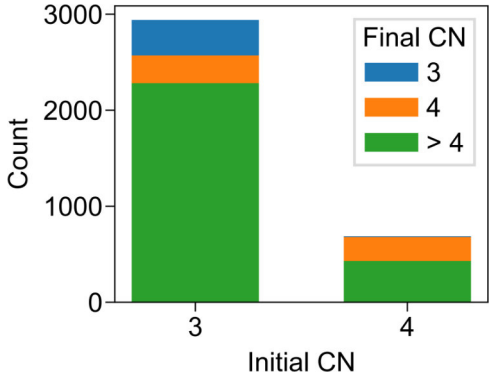

Figure S5: The change of coordination number (CN) of 3- and 4-coordinated configurations, which are rejected in the original simulations, upon structural relaxations.

To find an appropriate attempt frequency for accelerated kMC simulation, we check the convergence of loss quantity as we increase the attempt frequency from 10^4 Hz. We set the attempt frequency to 10^6 Hz because the attempt frequency of 10^6 Hz is high enough to describe the loss quantity as accurately as a higher attempt frequency (see Figure S6).

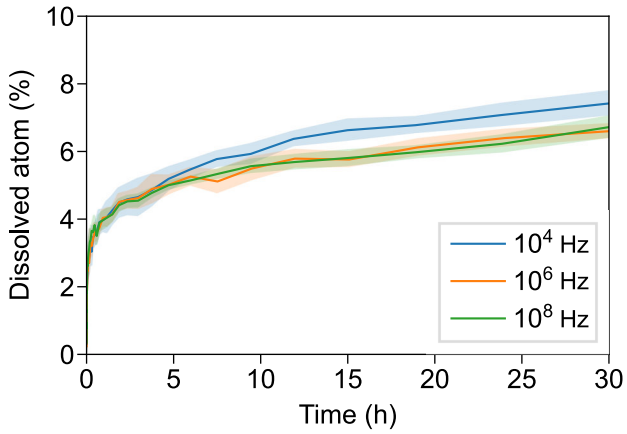

Figure S6: Diffusion attempt frequency convergence test.

Details of the training set

We have considered the following series of structures: i) distorted crystal structures with the lattice constant scaled with the range of 5% around the ground state of Pt, Pt_3Co, PtCo, $PtCo_3$, and Co, ii) MD snapshots, iii) vacancy diffusion pathways and iv) relaxation path of multi vacancy structures. For distorted crystals, FCC (also HCP, if needed) phases of all intermetallic compounds are calculated. The MD snapshots were sampled with an interval of 0.1 ps from the 15 ps 600 K NVT simulation with 1—2 vacancies for bulk and surface, respectively. The MD snapshots for the slab were taken from (100) and (111) slabs and the lattice vectors of the periodic xy plane were set by Vegard's law. For vacancy diffusion pathways, NEB calculations were done with 7 images. A vacancy pair was chosen for bulk multi-vacancy structures, up to the 4^{th} neighbor. The multi-vacancy structures were added to the training set to explain the vacancy-vacancy interactions. In order to efficiently sample diverse defect configurations, we ensure that the training structures in the same category (see Table S2) do not contain the same local environments of vacancies, which are defined by the composition of the nearest-neighbor atoms.

Table S2: Categories for comparing the Co composition of nearest neighbors for vacancies

Category index	Type	# of vacancies
1	Bulk	1
2	Bulk	2
3	Surface (100)	1
4	Surface (100)	2
5	Surface (100)	3
6	Surface (100)	4
7	Surface (111)	1
8	Surface (111)	2
9	Surface (111)	3
10	Surface (111)	4

We evaluated changes in vacancy formation energies across different alloy compositions, keeping the nearest-neighbor atoms fixed but varying the other atomic compositions. Figure S7 presents the mean vacancy formation energies, supplemented by standard deviations, for

configurations having identical nearest neighbors (Figures S7a and b represent the (100) and the (111) surface, respectively). The data reveals that the standard deviations of the vacancy formation energies are only 0.13 eV for the (100) surface and 0.10 eV for the (111) surface. These deviations are notably smaller than the variations seen in the vacancy formation energy across variable compositions (approximately 0.4 eV for both (100) and (111) surfaces, respectively).

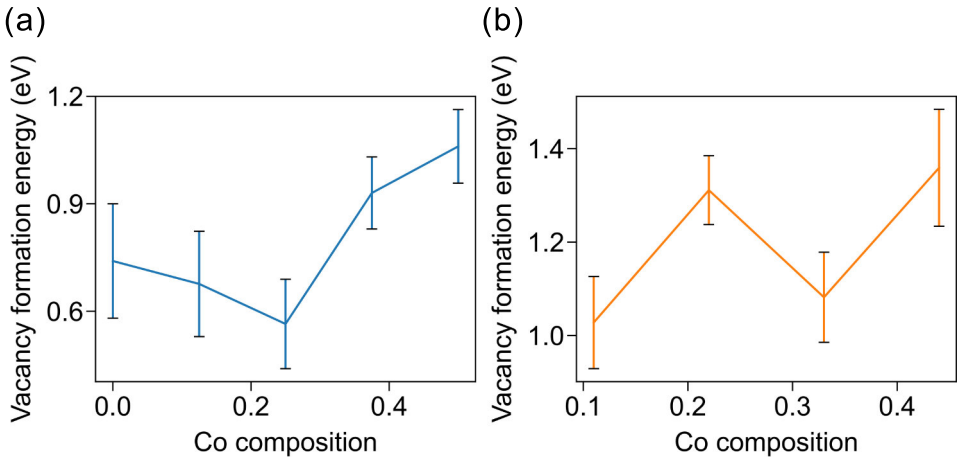

Figure S7: Variation of vacancy formation energy varying local environments. Vacancy formation energies on the (a) (100) and (b) (111) surface are shown. The error bar indicates the standard deviations of twenty independent samples.

We assessed the uncertainties of atomic configurations in the nanoparticle that appears in the kMC simulations (Figure S8a) employing the ensemble method.[S10] Uncertainty values are indeed instrumental in gauging how well atomic configurations are represented within the training set. To ascertain any sampling bias across energy levels, we plotted uncertainty against energy for the octahedron nanoparticles that emerge in the kMC simulation in Figures S8b and c (for Pt and Co, respectively). Our findings indicate that uncertainties remain reasonably low (0.144 eV/atom; 95^{th} percentile in the training set) for the majority of configurations, in all energy ranges. It is essential to highlight, though, that due to the atomic mapping characteristics of machine-learned potentials, these uncertainty values may not genuinely reflect the thermodynamic energy associated with each atom.[S11] Therefore,

the low-energy configurations are not necessarily the common configurations. Nevertheless, our analysis indicates that the sampling has been uniformly conducted across diverse energy ranges.

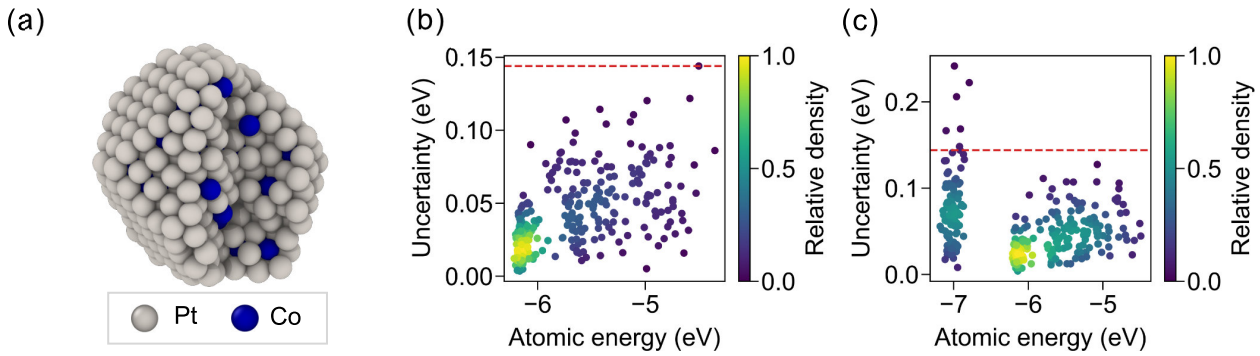

Figure S8: The uncertainty and atomic energy distribution on the nanoparticle from kMC simulation. (a) Atomic structure of the nanoparticle from kMC simulation. Correlation between atomic energies and uncertainties for (b) Pt and (b) Co atoms. The atomic structure is cut by a quarter to display its internal atomic arrangements. The red dashed line indicates the 95$^{\text{th}}$ percentile uncertainty value of the training set.

Table S3: Details of the training set

Structure type	Method	Composition ($Pt_{1-x}Co_x$)	Number of structures	Number of atoms	Number of training points
Bulk	Distortion	0.1	11	108	1,188
		0.25	11	108	1,188
		0.5	22	108	2,376
		0.75	11/44	108/96	5,412
		1.0	11/44	108/96	5,412
	MD (600 K)	0.0	30	107	3,210
		0.1	30	107	3,210
		0.2	30	107	3,210
		0.3	30	107	3,210

Continued on next page

Table S3 – continued from previous page

Structure type	Method	Composition ($Pt_{1-x}Co_x$)	Number of structures	Number of atoms	Number of training points
Bulk		0.4	30	107	3,210
		1.0	30	107	3,210
	NEB	0.0	22	107	2,354
		0.1	41	107	4,387
		0.2	43	107	4,601
		0.3	44	107	4,708
		0.4	49	107	5,243
		1.0	14	107	1,498
	Relaxation	0.0	5	106	530
		0.1	17	106	1,802
		0.2	20	106	2,120
		0.3	23	106	2,438
		0.4	25	106	2,650
		1.0	10	106	1,060
(100) surface	MD (600 K)	0.0	30	79	2,370
		0.1	30	78	2,340
		0.2	30	78	2,340
		0.3	30	78	2,340
		0.4	30	78	2,340
	NEB	0.0	54	79	4,266
		0.1	144	79	11,376
		0.2	113	79	8,927
		0.3	144	79	11,376

Continued on next page

Table S3 – continued from previous page

Structure type	Method	Composition ($Pt_{1-x}Co_x$)	Number of structures	Number of atoms	Number of training points
		0.4	203	79	16,037
(100) surface	Relaxation	0.0	21	104–106	2,203
		0.1	23	104–106	2,410
		0.2	21	104–106	2,210
		0.3	36	104–106	3,772
		0.4	32	104–106	3,365
(111) surface	MD (600 K)	0.0	30	79	2,370
		0.1	30	78	2,340
		0.2	30	78	2,340
		0.3	30	78	2,340
		0.4	30	78	2,340
	NEB	0.0	53	79	4,187
		0.1	107	79	8,453
		0.2	94	79	7,426
		0.3	213	79	16,827
		0.4	102	79	8,058
	Relaxation	0.0	27	92–94	2,511
		0.1	18	92–94	1,674
		0.2	22	92–94	2,045
		0.3	26	92–94	2,416
		0.4	29	92–94	2,697
Truncated octahedron	NEB	0.0	245	150	36,750
		0.25	120	150	18,000

Continued on next page

Table S3 – continued from previous page

Structure type	Method	Composition ($Pt_{1-x}Co_x$)	Number of structures	Number of atoms	Number of training points
Truncated octahedron	Relaxation	0.0	82	145–150	12,061
		0.25	102	145–150	15,008
Icosahedron	NEB	0.0	127	139	17,653
		0.25	140	139	19,460
	Relaxation	0.0	68	134–139	9,261
		0.25	58	134–139	7,895
Cuboctahedron	NEB	0.0	132	151	19,932
		0.25	132	151	19,932
	Relaxation	0.0	176	146–151	25,955
		0.25	134	146–151	19,822
Octahedron	NEB	0.0	129	127	16,383
		0.25	111	127	13,986
	Relaxation	0.0	267	122–127	33,040
		0.25	124	122–127	15,397
Total			4,576		514,449

Training quality of NNP

The trained NNP exhibits root-mean-square errors (RMSEs) of 4.46 meV/atom, 0.13 eV/Å, and 6.72 kbar for energy, force, and stress, respectively, for the validation set (see Figure S9).

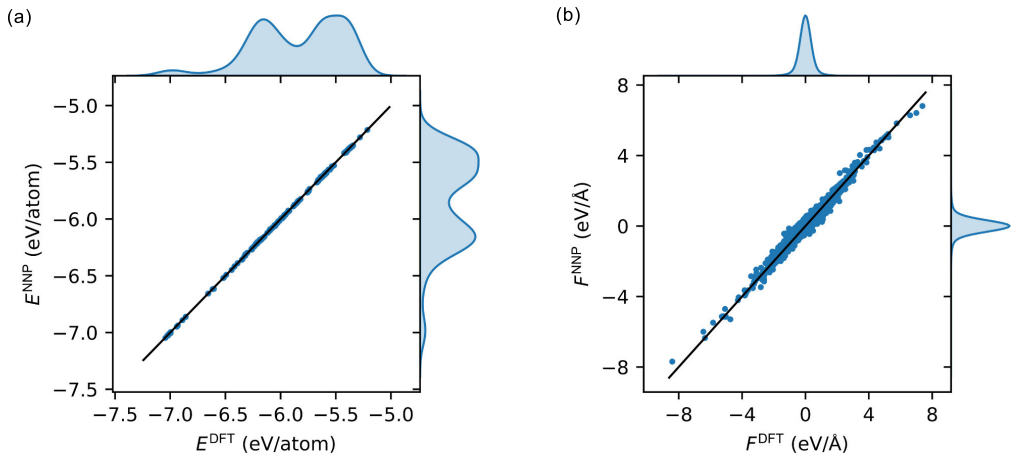

Figure S9: The parity plots for NNP and DFT. (a) Energy and (b) force correlation for the validation set.

Accuracy of the MEAM potential

MEAM potential[S12] has the RMSE of 0.381 eV and 0.835 eV for vacancy formation energy and migration barrier.

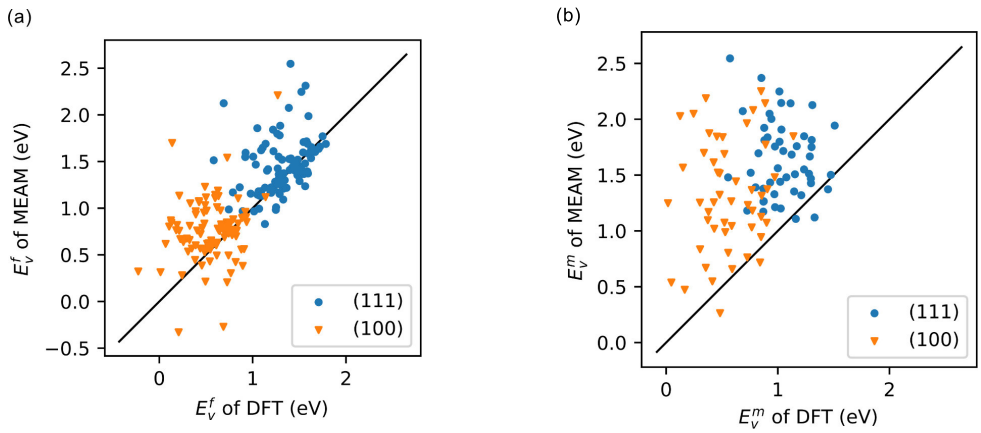

Figure S10: Performance test of the MEAM potential. (a) Vacancy formation energy (b) vacancy migration barrier

Error of surface and edge sites

We investigate the contribution of error sources from bulk, surface, edge, and vertex sites. However, due to the atomic mapping characteristics of machine-learned potentials,[S11] it is

difficult to directly pinpoint errors in individual atoms. Instead, we have calculated the uncertainty for each atomic site, which reflects how well the local environment around each atom is represented in the training set. The uncertainty is defined as a standard deviation of atomic energies, calculated from the ensemble of four machine-learned potentials trained on the atomic energies in the training set.[S10] High atomic uncertainties indicate that the corresponding local environment is not included in the training set, potentially leading to significant errors. Figures S11a-c show the uncertainties of edge (with vertex), surface (with subsurface), and bulk atoms, respectively, as a function of nanoparticle size. The red dashed line shows the uncertainty value for the 95^{th} percentile of the training set. In Figure S11a, we find that the uncertainties of edge and vertex atoms are lower than the uncertainties in the training set, which means that these configurations are sampled in the training set, except for the small nanoparticles with diameters lower than 1.0 nm. The uncertainties of surface and subsurface atoms are almost similar to the edge and vertex atoms (Figure S11b). The uncertainties of bulk atoms (Figure S11c) are marginally lower than those of the surface, edge, and vertex atoms, but with no significant differences. This suggests that the errors are not predominantly localized to the under-coordinated atoms at the edges and vertices but are instead dispersed throughout the entire nanoparticles. On the other hand, nanoparticles smaller than 1.0 nm still display substantial errors and uncertainties. To visualize the uncertainties in these nanoparticles, we have assigned colors to the atoms based on their uncertainty values in Figure S12. We observe that a significant portion of the nanoparticles exhibit uncertainties exceeding the values in the training set. This might be attributed to the presence of local environments with high vacuum ratios, which are not sampled in the original training set.

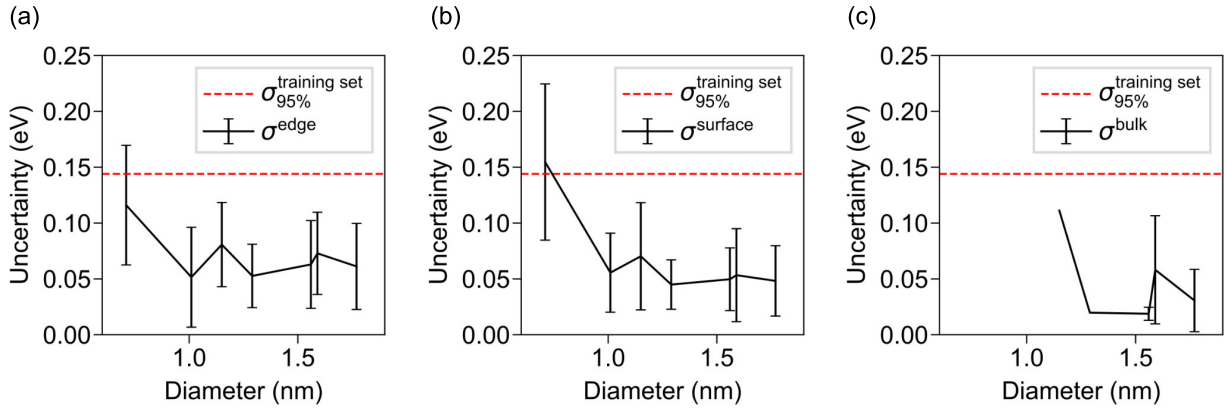

Figure S11: The uncertainty analysis for three different regions for varying sizes and shapes of nanoparticles. The regions in nanoparticles are divided into (a) edge (with vertex), (b) surface (with subsurface), and (c) bulk atoms. Error bars represent standard deviations. The red dashed line indicates the 95$^{\text{th}}$ percentile uncertainty value of the training set.

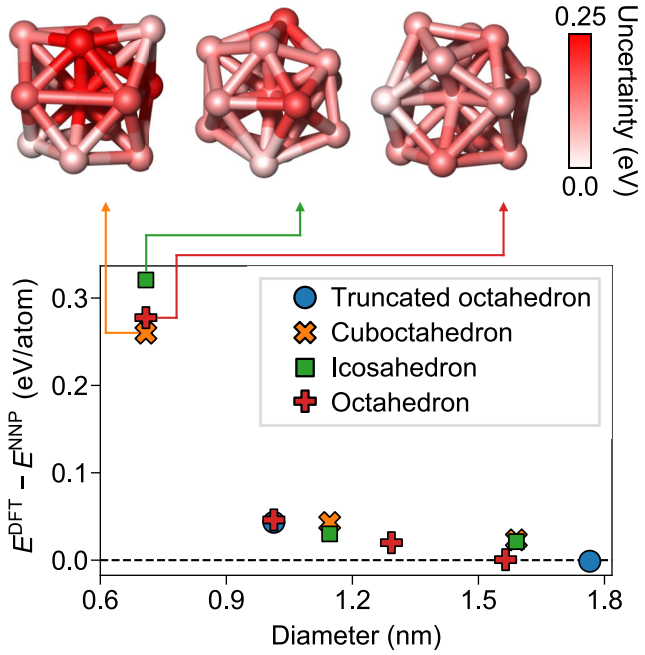

Figure S12: Errors in NNP across different sizes and shapes of nanoparticles. Insets provide a visual representation of nanoparticles smaller than 1 nm, with uncertainties indicated by color-coding.

NNP error on various shapes of nanoparticles

The NNP errors for the icosahedron, cuboctahedron, and octahedron shape of nanoparticles are evaluated.

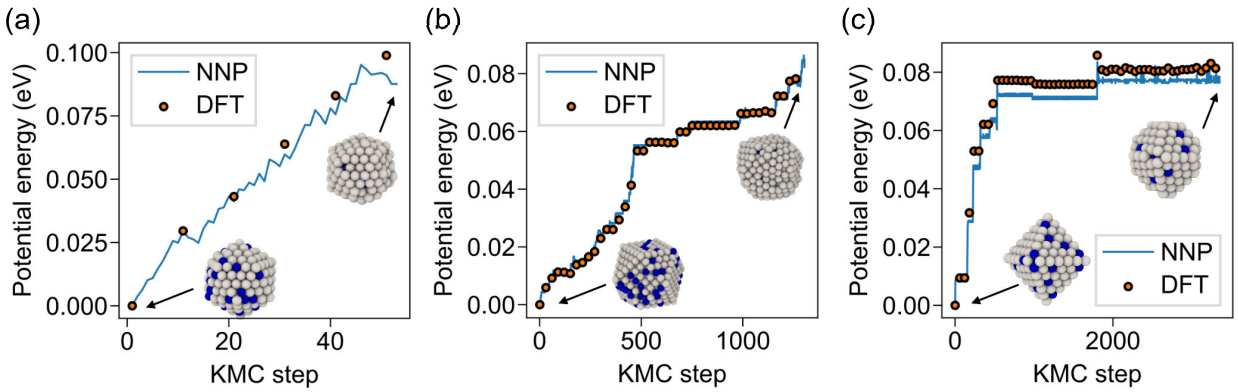

Figure S13: Single-point DFT calculations on the structure from kMC simulation. (a) icosahedron, (b) cuboctahedron, and (c) octahedron. The energies obtained from both NNP and DFT calculations are referenced to the energy of the first snapshot of the kMC simulation.

Derivation of total loss ratio

We derived theoretically the loss of the initial atoms as a function of particle diameter, using the reaction rate (k) and Gibbs–Thomson equation[S13] that is defined as:

$$\Delta E = -\frac{4\Omega}{n} \cdot \frac{\gamma}{d}, \tag{10}$$

where ΔE stands for change of dissolution potential, and Ω, n, γ, and d are the atomic volume, the number of electrons transferred, surface energy, and diameter of the particle. First, we can easily assume that the number of dissolved atoms is proportional to the number of surface atoms ($\sim d^2$) and the reaction rate of dissolution (k). Next, we rewrite the reaction rate (k) in terms of diameter (d) and activation barrier (E_a). According to the BEP relation, the activation barrier is proportional to the reaction energy. In our case, the change of dissolution potential (ΔE) can be regarded as reaction energy. Therefore, the loss becomes

a function of diameter (d) and change of dissolution potential (ΔE). Finally, the change of dissolution potential is inversely proportional to diameter based on the Gibbs–Thomson equation, making the loss of initial atoms only a function of diameter.

$$\text{Loss}(\%) \propto \frac{d^2 \times k}{d^3} \tag{11}$$

$$\propto \frac{A}{d} \exp\left(-\frac{E_a}{k_B T}\right) \tag{12}$$

$$\propto \frac{A}{d} \exp\left(-B\Delta E\right) \tag{13}$$

$$= \frac{A}{d} \exp\left(\frac{B}{d}\right) \tag{14}$$

Comparison of icosahedrons and octahedrons

Octahedrons have lower vacancy formation energy of the edge sites than icosahedrons.

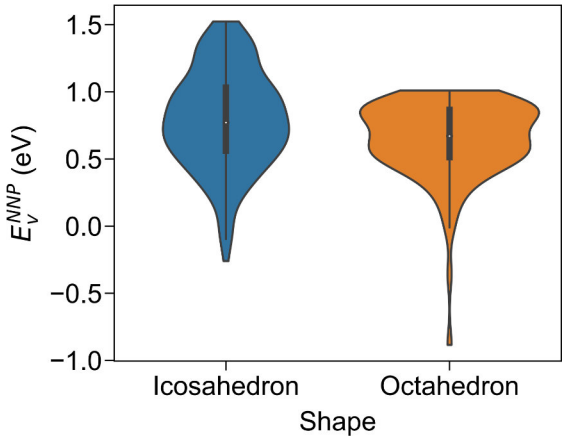

Figure S14: Vacancy formation energy of edge site for icosahedrons and octahedrons. The means (standard deviations) of vacancy formation energy for icosahedron and octahedron are 0.79 eV (0.36 eV) and 0.64 eV (0.29 eV), respectively.

Extending the elemental systems

The trends in durability in relation to the size, shape, and atomic ordering of Pt_3Ni nanoparticles are also similar to those of Pt_3Co nanoparticles (see Figures S15a-c). Note that we

assume that the BEP parameters of Co and Ni are identical due to their similar electrochemical characteristics.[S14]

Table S4: Energy and force RMSE for PtNi and PtCoNi systems

System	Energy RMSE (meV/atom)	Force RMSE (eV/Å)
PtNi	2.6	0.13
PtCoNi	3.3	0.12

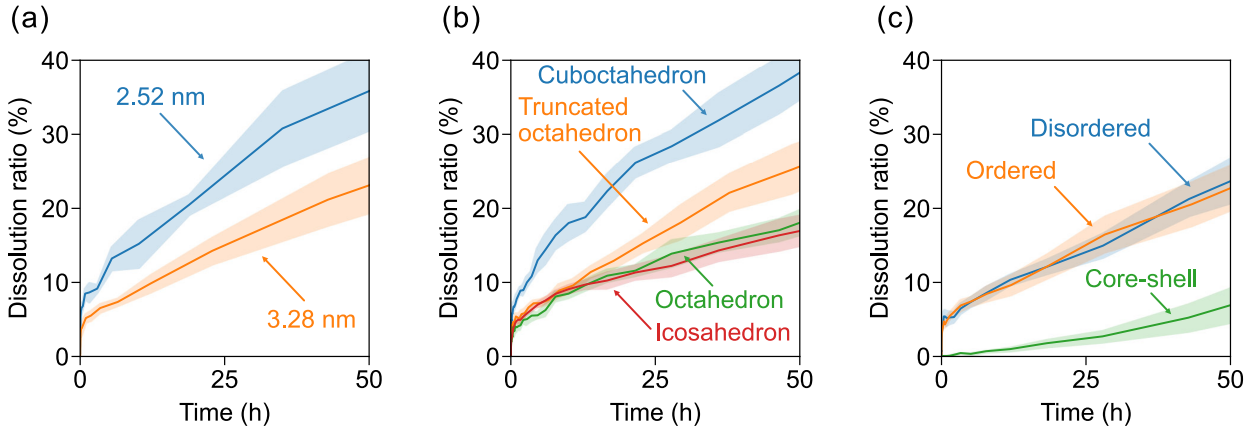

Figure S15: KMC simulation results for PtNi. (a) Time evolution of dissolution ratio of various sizes of truncated octahedron Pt_3Ni nanoparticles. The dissolution ratio is defined as a ratio of the number of dissolved atoms to that of the initial total atoms. (b) Time evolution of dissolution ratio of various shapes of Pt_3Ni nanoparticles. (c) Time evolution of dissolution ratio of ordered, disordered, and core–shell Pt_3Ni nanoparticles.

References

(S1) Mathew, K.; Sundararaman, R.; Letchworth-Weaver, K.; Arias, T. A.; Hennig, R. G. Implicit solvation model for density-functional study of nanocrystal surfaces and reaction pathways. *J. Chem. Phys.* **2014**, *140*, 084106.

(S2) Mathew, K.; Kolluru, V. S. C.; Mula, S.; Steinmann, S. N.; Hennig, R. G. Implicit self-consistent electrolyte model in plane-wave density-functional theory. *J. Chem. Phys.* **2019**, *151*, 234101.

(S3) Evans, M. G.; Polanyi, M. Inertia and driving force of chemical reactions. *Trans. Faraday Soc.* **1938**, *34*, 11–24.

(S4) Seo, J. K.; Khetan, A.; Seo, M. H.; Kim, H.; Han, B. First-principles thermodynamic study of the electrochemical stability of Pt nanoparticles in fuel cell applications. *J. Power Sources* **2013**, *238*, 137–143.

(S5) Ahluwalia, R. K.; Papadias, D. D.; Kariuki, N. N.; Peng, J.-K.; Wang, X.; Tsai, Y.; Graczyk, D. G.; Myers, D. J. Potential dependence of Pt and Co dissolution from platinum-cobalt alloy PEFC catalysts using time-resolved measurements. *J. Electrochem. Soc.* **2018**, *165*, F3024–F3035.

(S6) Gu, G. H.; Lim, J.; Wan, C.; Cheng, T.; Pu, H.; Kim, S.; Noh, J.; Choi, C.; Kim, J.; Goddard, W. A.; Duan, X.; Jung, Y. Autobifunctional mechanism of jagged Pt nanowires for hydrogen evolution kinetics via end-to-end simulation. *J. Am. Chem. Soc.* **2021**, *143*, 5355–5363.

(S7) Erlebacher, J. An atomistic description of dealloying. *J. Electrochem. Soc.* **2004**, *151*, C614.

(S8) Hrnjic, A.; Kamšek, A. R.; Pavlišič, A.; Šala, M.; Bele, M.; Moriau, L.; Gatalo, M.; Ruiz-Zepeda, F.; Jovanovič, P.; Hodnik, N. Observing, tracking and analysing electrochemically induced atomic-scale structural changes of an individual Pt−Co nanoparticle as a fuel cell electrocatalyst by combining modified floating electrode and identical location electron microscopy. *Electrochim. Acta* **2021**, *388*, 138513.

(S9) González, A. Measurement of areas on a sphere using Fibonacci and latitude−longitude lattices. *Math. Geosci.* **2010**, *42*, 49.

(S10) Jeong, W.; Yoo, D.; Lee, K.; Jung, J.; Han, S. Efficient atomic-resolution uncertainty estimation for neural network potentials using a replica ensemble. *J. Phys. Chem. Lett.* **2020**, *11*, 6090–6096.

(S11) Yoo, D.; Lee, K.; Jeong, W.; Lee, D.; Watanabe, S.; Han, S. Atomic energy mapping of neural network potential. *Phys. Rev. Mater.* **2019**, *3*, 093802.

(S12) Kim, J.-S.; Seol, D.; Lee, B.-J. Critical assessment of Pt surface energy − an atomistic study. *Surf. Sci.* **2018**, *670*, 8–12.

(S13) Plieth, W. J. Electrochemical properties of small clusters of metal atoms and their role in the surface enhanced Raman scattering. *J. Phys. Chem.* **1982**, *86*, 3166–3170.

(S14) Colón-Mercado, H. R.; Popov, B. N. Stability of platinum based alloy cathode catalysts in PEM fuel cells. *J. Power Sources* **2006**, *155*, 253–263.